

LINEARISED FREQUENCY DOMAIN GUST ANALYSIS OF LARGE CIVIL AIRCRAFT

P. Bekemeyer¹, R. Thormann² and S. Timme³

¹Ph.D. Student
University of Liverpool
e-mail: philipp.bekemeyer@liverpool.ac.uk

²Research Associate and ³Lecturer
University of Liverpool
e-mail: {reik.thormann,sebastian.timme}@liverpool.ac.uk

Keywords: Large Civil Aircraft, Gust Response, Frequency Domain, Computational Fluid Dynamics, Reynolds-averaged Navier-Stokes Equations

Abstract. *Predicting loads due to atmospheric turbulence is crucial in the aircraft design and certification process. Efficient methods are important regarding the large number of simulations needed to cover the parameter space of e.g. Mach number, flight altitude and gust shape. Since commercial aircraft operate at transonic flight speeds, applied methods should consider aerodynamic nonlinearities such as shocks and boundary layer separation. Based on a recently presented method using frequency domain computational fluid dynamics for gust interaction, an extension towards industry-relevant three-dimensional cases is proposed. Results are shown for a large civil aircraft solving the Reynolds-averaged Navier-Stokes equations. Complex-valued surface pressures from time-linearised simulations are compared to nonlinear unsteady time-marching investigations. Responses to 1-cos gusts are obtained to discuss time histories of load factors and worst case surface pressure distributions.*

1 INTRODUCTION

Various dynamic response simulations need to be performed in order to achieve aircraft certification. Fast and reliable prediction tools are required to analyse several different gust parameters and flight conditions. Furthermore, aerodynamic nonlinearities, e.g. recompression shocks and shock induced boundary layer separation, should be considered to accurately predict loads. Current industrial practice is based on potential flow equations, mostly the doublet lattice method (DLM) [1], which predicts unsteady aerodynamic loads uncoupled from the steady flowfield. Gust loads are included using a frequency domain sampling and projecting surface forces on structural modes. While this offers fast predictions throughout the flight envelope, aerodynamic nonlinearities are neglected. At transonic flow conditions in particular, DLM is not predicting loads conservatively and thus DLM correction methods or more accurate tools need to be applied.

Recently computational fluid dynamics (CFD) has become more interesting for loads prediction, offering accurate results also at aforementioned nonlinear conditions. While unsteady time-marching gust simulations are technically possible also for large configurations [2], they are currently not feasible in an industrial environment due to overwhelming computational cost. However, linear frequency domain based methods, also known as time-linearised methods, have shown large runtime improvements while maintaining the accuracy of the underlying nonlinear CFD model [3]. More commonly used for forced-motion simulations, an extension towards gust excitation has been presented recently for the Reynolds-averaged Navier-Stokes (RANS) equations [4]. Results are shown for an aerofoil at subsonic and transonic flight conditions. Aerodynamic responses to 1-cos gusts are obtained by superposing several frequency domain results at discrete frequencies deploying a real-valued weighting function.

First applications for time-linearised methods were demonstrated in the field of turbomachinery [5, 6, 7]. Assuming harmonic blade motion of small amplitude, the Euler equations are linearised around a nonlinear steady-state solution. Solving then for the first harmonic is offering huge time savings compared to a time-marching approach [8, 9]. Considering external flows, initial results for an aerofoil are presented in [10]. Forced motion responses are shown for an aerofoil, wing and an aircraft in [11], while a delta wing under small harmonic oscillations of elastic modes as well as control surfaces is discussed in [12]. Compared to solving the unsteady nonlinear Euler equations in a time-marching approach, a significant speed-up is reported throughout, independent of the techniques applied to solve the resulting linear systems of equations.

Considering the RANS equations, initial work has again been published for turbomachinery applications [13]. Stall flutter including large separation regions inside a blade cascade is investigated with good agreement to experimental data. For external flows, analysing forced-motion responses, time-saving factors between one and two orders of magnitude have been demonstrated for aerofoils and wings [14, 15]. Regarding a full civil aircraft at cruise conditions speed-up of nearly two orders of magnitude has been reported [16].

In this paper an application of the linear frequency domain method for gust solving the RANS equations is demonstrated for a full aircraft configuration including fuselage, wing, tail and nacelles. Unsteady results are presented for a transonic Mach number after a steady elastic trimming process. Aerodynamic responses to sinusoidal gusts are compared to their time domain counterparts while discussing accuracy and efficiency of both methods. Finally, responses to several 1-cos gusts, based on international certification requirements, are evaluated in a very efficient way by exploiting the consolidated frequency domain technique.

2 METHODS

The nonlinear governing equation in semi-discrete form is written as

$$\dot{\mathbf{w}} = \mathbf{R}(\mathbf{w}, \mathbf{v}_g) \quad (1)$$

where \mathbf{w} is the state-space vector of unknowns, \mathbf{R} denotes the nonlinear residual corresponding to the unknowns and \mathbf{v}_g describes external disturbances due to gusts.

The difference between an equilibrium solution \mathbf{w}_0 and the instantaneous state-space vector \mathbf{w} is introduced as

$$\Delta \mathbf{w} = \mathbf{w} - \mathbf{w}_0 \quad (2)$$

and accordingly for external disturbances. A first order Taylor expansion is used to express the residual in Eq. (1) around the equilibrium point assuming small perturbations

$$\Delta \dot{\mathbf{w}} = \mathbf{R}(\mathbf{w}_0, \mathbf{v}_{g0}) + \frac{\partial \mathbf{R}}{\partial \mathbf{w}} \Delta \mathbf{w} + \frac{\partial \mathbf{R}}{\partial \mathbf{v}_g} \Delta \mathbf{v}_g \quad (3)$$

where $A = \frac{\partial \mathbf{R}}{\partial \mathbf{w}}$ denotes the Jacobian matrix. The first term on the right-hand side of the latter equation is by definition zero and equivalent to the nonlinear steady flow solution that accounts for aerodynamic nonlinearities.

Subsequently, the system is transferred into frequency domain assuming the disturbance vector $\Delta \mathbf{w}$ and external excitation vector $\Delta \mathbf{v}_g$ change harmonically in time. After rearranging, Eq. (3) becomes

$$(A - i\omega I) \hat{\mathbf{w}} = -\Xi(\omega) \frac{\partial \mathbf{R}}{\partial \mathbf{v}_g} \hat{\mathbf{v}}_g \quad (4)$$

with $\hat{\mathbf{w}}$ and $\hat{\mathbf{v}}_g$ as complex-valued Fourier coefficients.

The response to an arbitrary time domain signal is obtained by superposing frequency domain responses with the complex-valued weights denoted $\Xi(\omega)$ ¹. In Fig. 1 the time and frequency domain representations for three different excitation types are shown. While the sinusoidal excitation only needs one single frequency domain solve, the two other signals affect an infinite range of frequencies. Comparing the 1-cos and pulse excitation it can be seen that the pulse omits zero amplitudes, making it possible to excite all frequencies of interest with a single unsteady time-marching simulation. Obtained frequency domain results are then used to reconstruct the time history of the loads by applying an incomplete inverse Fourier transform. Furthermore, it is also possible to get the time history of the complete flowfield.

The right-hand side in Eq. (4) can be modified by applying the chain rule. Neglecting the weighting factor $\Xi(\omega)$ it becomes

$$\frac{\partial \mathbf{R}}{\partial \mathbf{v}_g} \hat{\mathbf{v}}_g = \frac{\partial \mathbf{R}}{\partial \dot{\mathbf{x}}} \frac{\partial \dot{\mathbf{x}}}{\partial \mathbf{v}_g} \hat{\mathbf{v}}_g \quad (5)$$

where $\dot{\mathbf{x}}$ denotes artificial mesh velocities applied to model the gust during the CFD calculation using the field velocity approach [17]. Since the relation between gust disturbance \mathbf{v}_g and artificial mesh velocity $\dot{\mathbf{x}}$ is simply

$$\dot{\mathbf{x}} = -\mathbf{v}_g \quad (6)$$

¹Compared to previously presented work in [4] this paper applies complex-valued weighting functions. While resulting in a slightly different analytical gust expression, this offers a further improvement in terms of computational efficiency since samples at discrete frequencies can be re-used to reconstruct an arbitrary time signal.

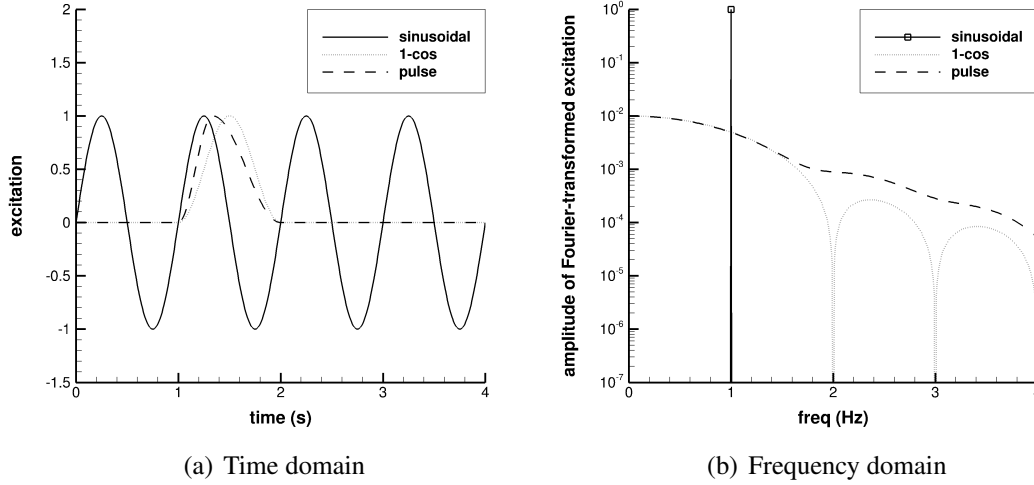


Figure 1: Excitation representation in time and frequency domain

Eq. (5) becomes

$$\frac{\partial \mathbf{R}}{\partial \mathbf{v}_g} \hat{\mathbf{v}}_g = -\frac{\partial \mathbf{R}}{\partial \mathbf{x}} \hat{\mathbf{v}}_g \quad (7)$$

The derivative in Eq. (7) is computed using a finite difference evaluation, applied around the equilibrium point, with a known gust shape vector $\hat{\mathbf{v}}_g$. Thus Eq. (7) becomes

$$\frac{\partial \mathbf{R}}{\partial \mathbf{v}_g} \hat{\mathbf{v}}_g = \frac{\mathbf{R}(+\varepsilon \mathbf{v}_g) - \mathbf{R}(-\varepsilon \mathbf{v}_g)}{2\varepsilon} \quad (8)$$

with ε denoting the finite difference step size. Two additional residual solves are necessary to construct the right-hand side before solving the linear system, while forming and storing the matrix $\frac{\partial \mathbf{R}}{\partial \mathbf{x}}$ explicitly can be avoided.

Furthermore, an analytical description for the gust vector is introduced as

$$\hat{\mathbf{v}}_g(\mathbf{x}, \omega) = v_{gz} e^{i\varphi(\mathbf{x}, \omega)} \quad (9)$$

where v_{gz} and $\varphi(\mathbf{x}, \omega)$ are the constant gust amplitude in z-direction and the phase shift at every mesh point, respectively. The phase shift can either be obtained from a Fourier analysis of the time domain signal or more elegantly using the analytical expression

$$\varphi(\mathbf{x}, \omega) = (\mathbf{x} + x_0) \omega \quad (10)$$

where x_0 represents the distance between gust and aircraft. The relation between the angular frequency ω and gust length of interest L_g is simply

$$\omega = \frac{2\pi U_\infty}{L_g} \quad (11)$$

with U_∞ as freestream velocity. Similar expressions can be derived for horizontal gusts by considering the corresponding amplitude and modifying the phase shift accordingly.

Results are produced using the DLR-TAU code [18] solving the RANS equations in conjunction with the Spalart-Allmaras turbulence model [19]. Fluxes are discretised applying the

Jameson-Schmidt-Turkel scalar artificial dissipation scheme [20]. Steady-state solutions are obtained utilising the backward Euler method with LU-SGS iteration [21]. For steady-state as well as unsteady simulations a 2v multigrid scheme is employed. Nonlinear time-marching solutions are computed using dual time-stepping of second order accuracy considering 128 steps per period. In addition, a Cauchy convergence criterion with an abort value of 10^{-8} for the relative error on drag coefficient is used to speed-up nonlinear time domain simulations. Gusts are introduced by adding an artificial mesh velocity during each time step which is prescribed according to the investigated gust shape [17]. Convergence for all linearised systems is achieved with a preconditioned generalised conjugate residual solver with deflated restarting [22]. For preconditioning a block incomplete lower upper factorisation of the approximate Jacobian matrix A with zero level of fill-in is applied [23]. The number of Krylov vectors necessary to solve each linear system is chosen based on engineering judgement and the guidelines published in [22], resulting in 100 vectors of which 20 are part of the deflated restarting process.

3 RESULTS

Results considering a large civil aircraft encountering either sinusoidal or 1-cos gusts are presented. First, convergence behaviour of the linear system is analysed and the influence of the finite difference step size ε is assessed. Then, several frequency domain gust responses at different frequencies are compared to corresponding nonlinear time domain simulations to outline the capability of the method for complex three-dimensional geometries. Therefore, complex surface pressure distributions are evaluated as well as representative sections on the wing and elevator. Finally, different 1-cos gust signals, chosen according to international certification requirements, are discussed. Besides time histories for the load factor n_z , also instantaneous surface pressure distributions corresponding to maximum load factor are reconstructed.

The investigated test case is a civil aircraft with a wingspan of approximately 60 m including elevator and fin. The computational mesh comprises nearly 8 million points of which 130,000 are on the surface. During the steady-state simulation at transonic flight conditions an elastic trimming is performed so that the lift balances the weight and zero pitching moment occurs. Elastic effects are captured using the first 94 structural modes while rigid-body modes are neglected. The trimming process is based on Broyden's method and adjusts angle of attack and elevator deflection iteratively until the desired coefficients are reached. Within each iterative trimming step, surface loads are calculated and the elastic deformation is updated accordingly. Subsequently, the density residual is driven to converge seven order of magnitude. The resulting surface shape in comparison to the undeformed aircraft is shown in Fig. 2(a). The most amplified structural modes are first wing bending and first wing twist, causing a decrease in sectional lift towards the wing tip. The corresponding surface pressure distribution is displayed in Fig. 2(b) with a strong shock visible along the wing span at roughly 70% chord length. On the elevator a suction area around the leading edge, but no shock formation, is present.

3.1 Investigation of Numerical Accuracy and Computational Cost

The convergence behaviour of the frequency domain solve is investigated first. A gust length of $L_g = 100$ m and an amplitude of 0.01% of the freestream velocity is chosen to ensure a dynamically linear response. While the linearity criterion can be relaxed as shown in Sec. 3.2, it is selected here to demonstrate the exact reproduction between time and frequency domain results. The convergence of the density residual, shown in Fig. 3(a), together with the magnitude of the lift coefficient normalised by its final value, confirms that even for this complex geometry

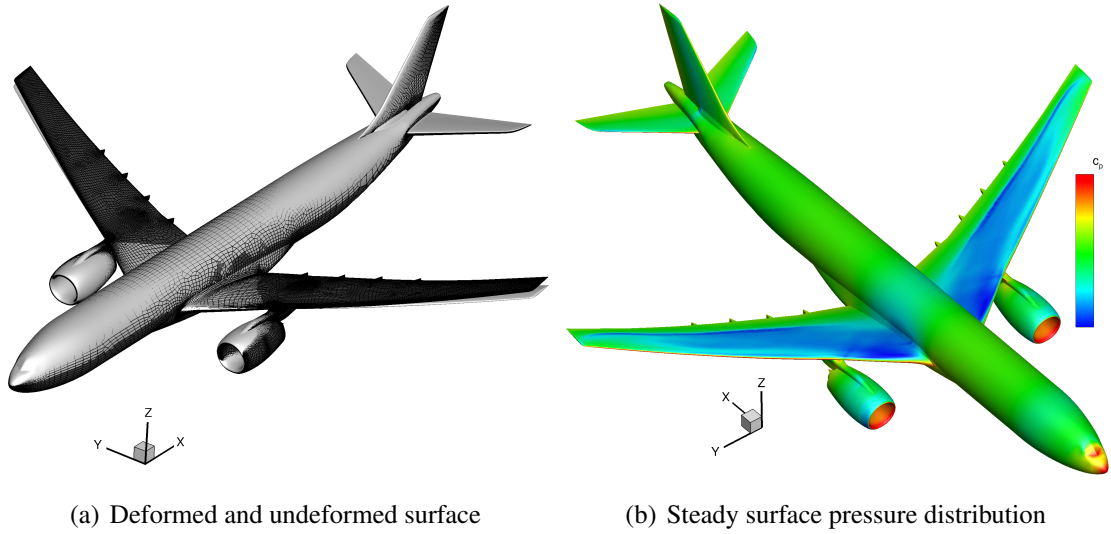


Figure 2: Deformed surface and steady-state surface pressure coefficient for civil aircraft

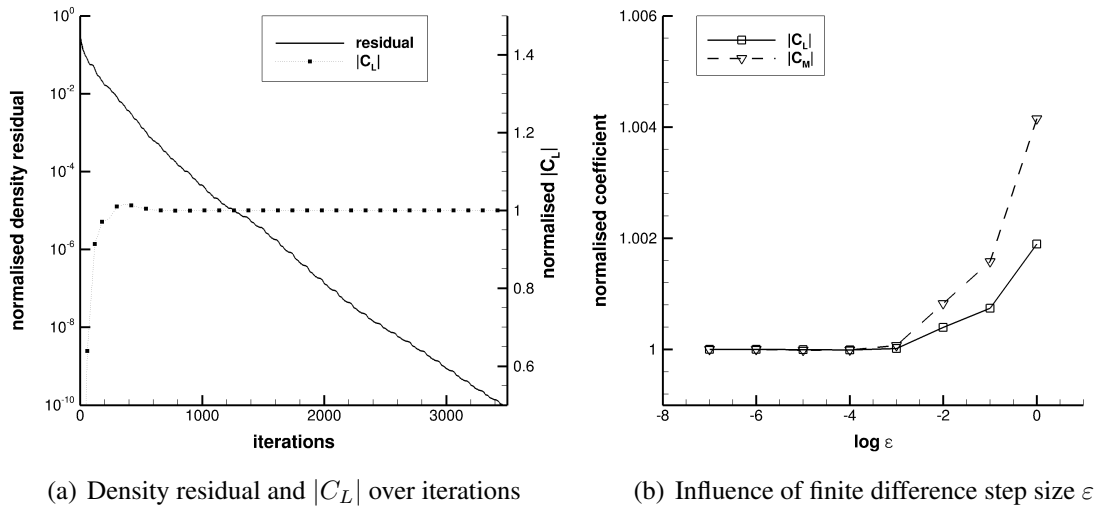
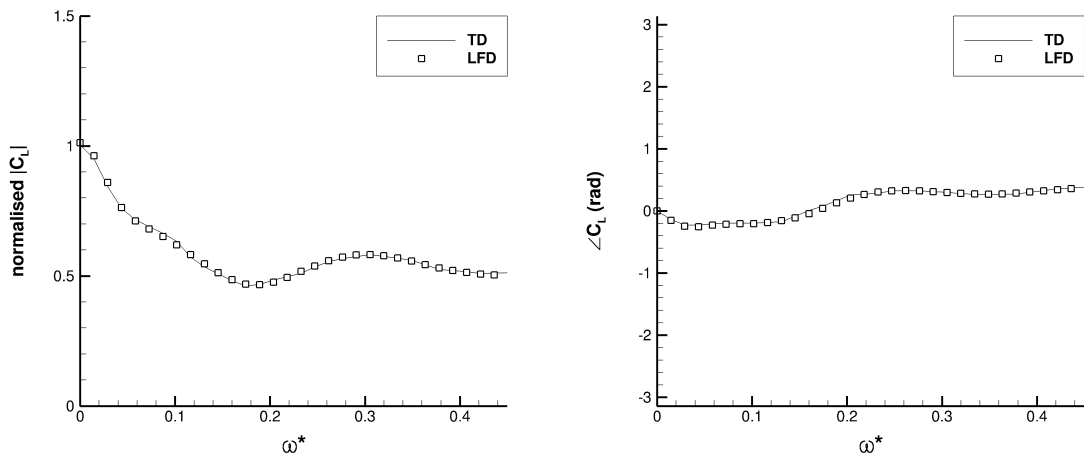


Figure 3: Numerical investigation of frequency domain gust approach

it is possible to converge to machine precision. The lift coefficient remains unchanged once the residual has converged four orders of magnitude. If only integrated loads are of interest, this offers time savings of additional 50% compared to aiming for full convergence. Subsequently, the abort criteria of six orders of magnitude based on the density residual is used, resulting in converged solutions for integrated loads as well as surface pressures.

The influence of the finite difference step size ε for forming the right-hand side in Eq. (8) is analysed next, investigating the same test case. The magnitudes of lift and pitching moment, presented in Fig. 3(b), are both normalised so that they converge towards one for small ε . Below $\varepsilon = 10^{-3}$ both coefficients are independent of the step size, while larger step sizes cause magnitudes to increase with a higher impact on the moment. A step size of 10^{-4} is then used throughout, ensuring results are independent of the step size.

The proposed method is validated at several frequencies by comparing frequency response functions of lift coefficient between time domain (TD) and linear frequency domain (LFD).



(a) Magnitude of lift frequency response function (b) Phase of lift frequency response function

Figure 4: Complex-valued frequency response functions of lift for time and frequency domain

Instead of producing time domain solutions separately for each frequency of interest, a pulse signal is used to excite all frequencies at once with one unsteady simulation. Then, a Fourier transform of the unsteady lift coefficient is performed and resulting complex-valued Fourier coefficients are weighted by the Fourier transform of the input signal. The amplitude of the excitation during the unsteady simulation is set to 0.01% of the freestream velocity, ensuring a linear dynamic response. Good agreement between time and frequency domain is observed for the magnitude normalised using the quasi steady result and phase of lift coefficient as can be seen in Figs. 4(a) and 4(b).

For a further validation complex-valued surface pressure distributions are compared between both methods for a gust length of $L_g = 100$ corresponding to a reduced frequency of about 0.073. While the frequency domain results are readily available after the linear system is solved, time domain solutions are generated in a similar fashion like the transfer function of lift coefficient. During the time-marching simulation the instantaneous surface pressure distributions are stored and then used in a Fourier transform. Results for the starboard wing are visualised in Figs. 5(a) and 5(b) for magnitude and phase with solid and dashed lines denoting time and frequency domain solutions, respectively. Good agreement between both methods at all locations, even at severe flow topologies, is obtained. The highest amplified region is around the shock at 70% chord length on the upper surface again with no differences between the simulations. Also around the wing-pylon junction, causing complex flow topologies due to vortices, excellent agreement is observed. Some minor discrepancies arise between the wing-fuselage junction in magnitude as well as phase. In Figs. 5(c) and 5(d) results are compared for the elevator and fin with similar good agreement. Highest magnitudes are located around the leading edge caused by the suction area since no shock formation is present. The phase is nearly constant on the elevator but shows large gradients near the trailing edge and during the transition from elevator leading edge to fuselage.

Values are extracted from the wing and elevator surface to compare time and frequency domain results in more detail, the locations of which are indicated by black lines in Fig. 5. Pressure magnitudes are scaled by the maximum value of the corresponding section while the x-axis is normalised by the local chord length. The first location is at 75% semi wingspan and

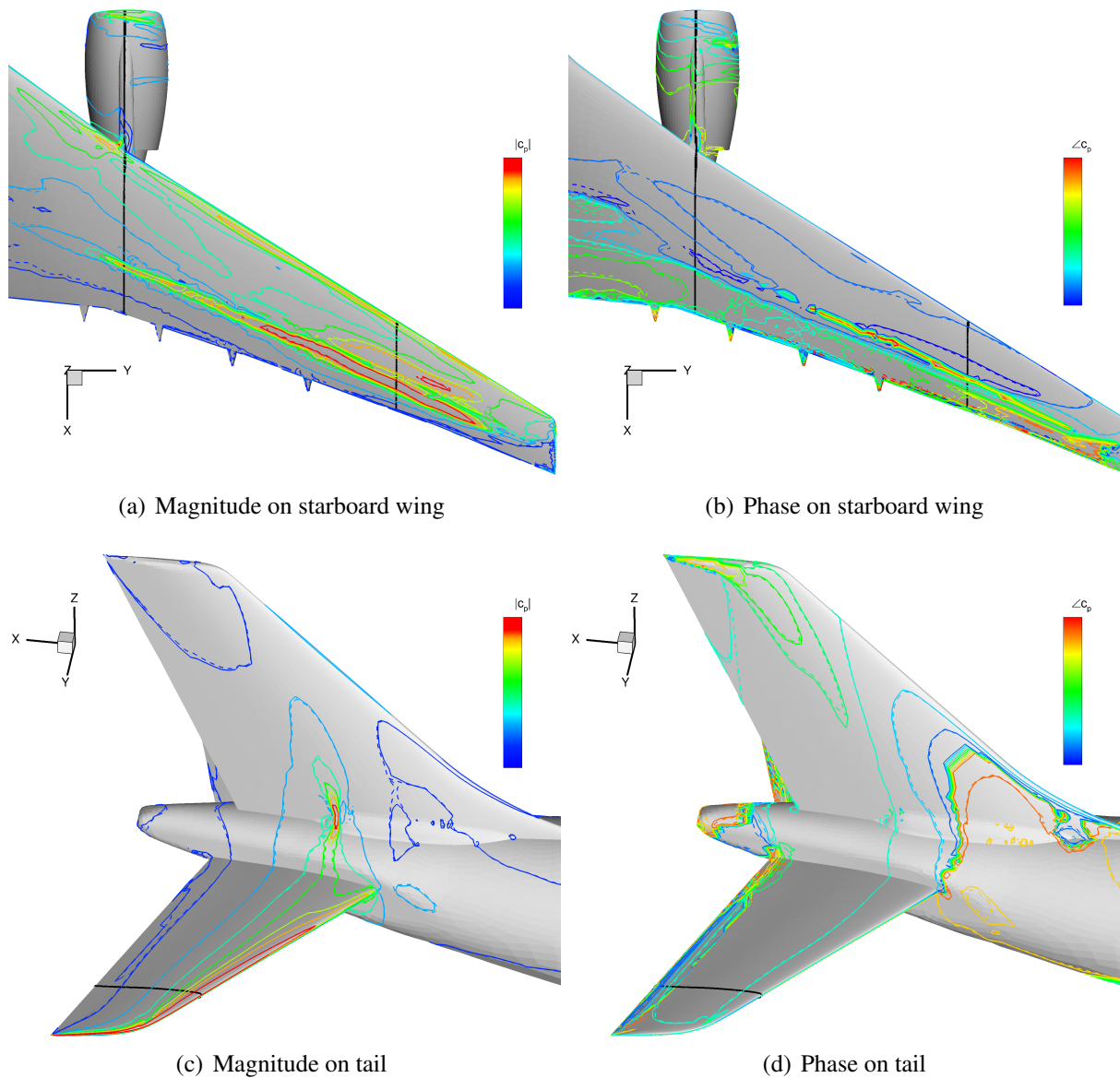
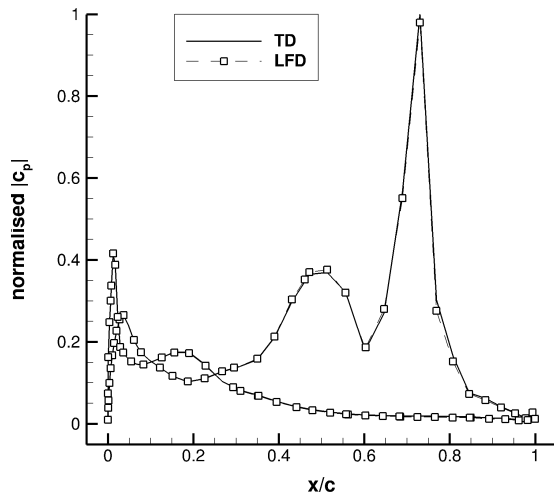
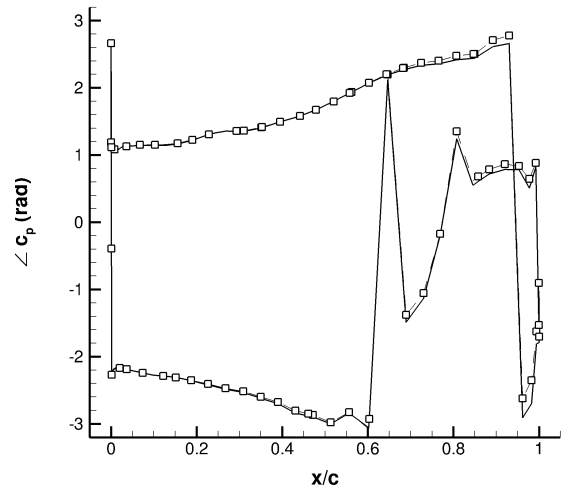


Figure 5: Complex-valued surface pressure with solid and dashed lines as time and frequency domain solution, respectively. Black lines show location of extracted sections

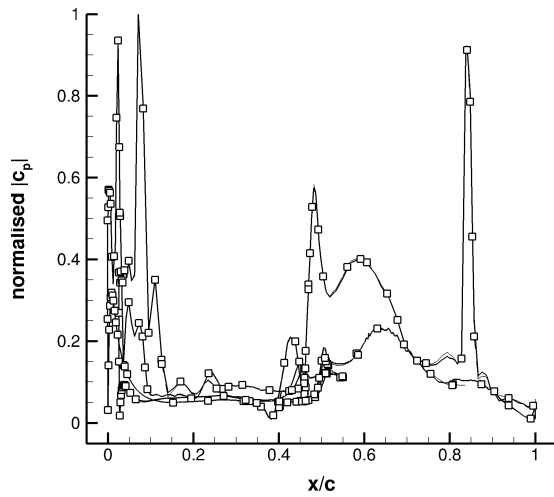
contains complex-valued pressures around the strong shock on the upper surface. Results for magnitude and phase are shown in Figs. 6(a) and 6(b) with good agreement. A small offset at the shock location is observed for phase with values being slightly overpredicted by the frequency domain method. For the second section at 32% semi wingspan magnitude and phase are compared in Figs. 6(c) and 6(d), respectively. Even in such complex flow situation due to the junction of wing, pylon and nacelle both methods are in excellent agreement. As in the previous section, similar behaviour can be seen for phase with small differences on the wing around the shock location. The third slice at 75% semi elevator span is displayed in Figs. 6(e) and 6(f). In contrast to surface pressures on the main wing, no shock formation is present, resulting in maximum values around the suction area instead. As before, a nearly perfect agreement for magnitude between both methods is found, while minor differences for phase occur around the trailing edge since the time-marching simulation is predicting a slightly steeper gradient.



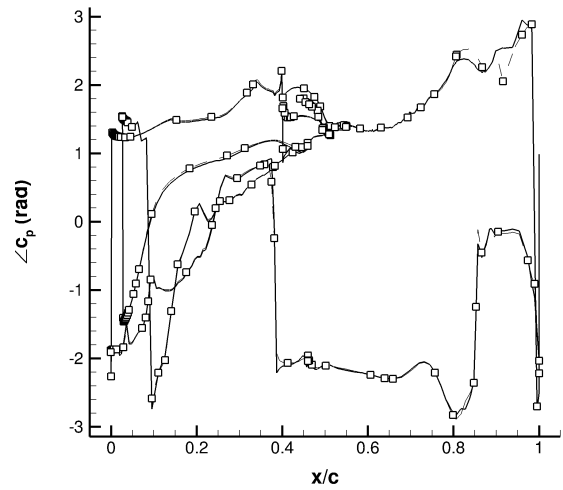
(a) Magnitude at 75% semi wingspan



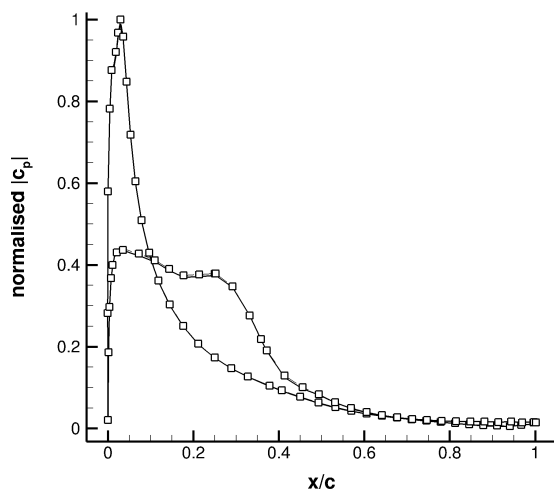
(b) Phase at 75% semi wingspan



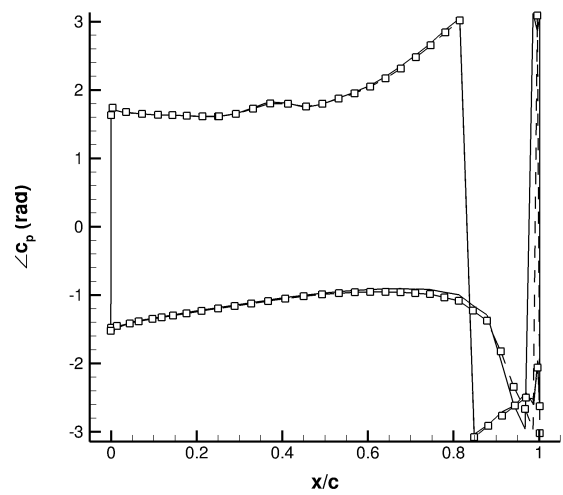
(c) Magnitude at 32% semi wingspan



(d) Phase at 32% semi wingspan



(e) Magnitude at 75% semi elevatorspan



(f) Phase at 75% semi elevatorspan

Figure 6: Complex-valued pressure distributions at wing and elevator sections

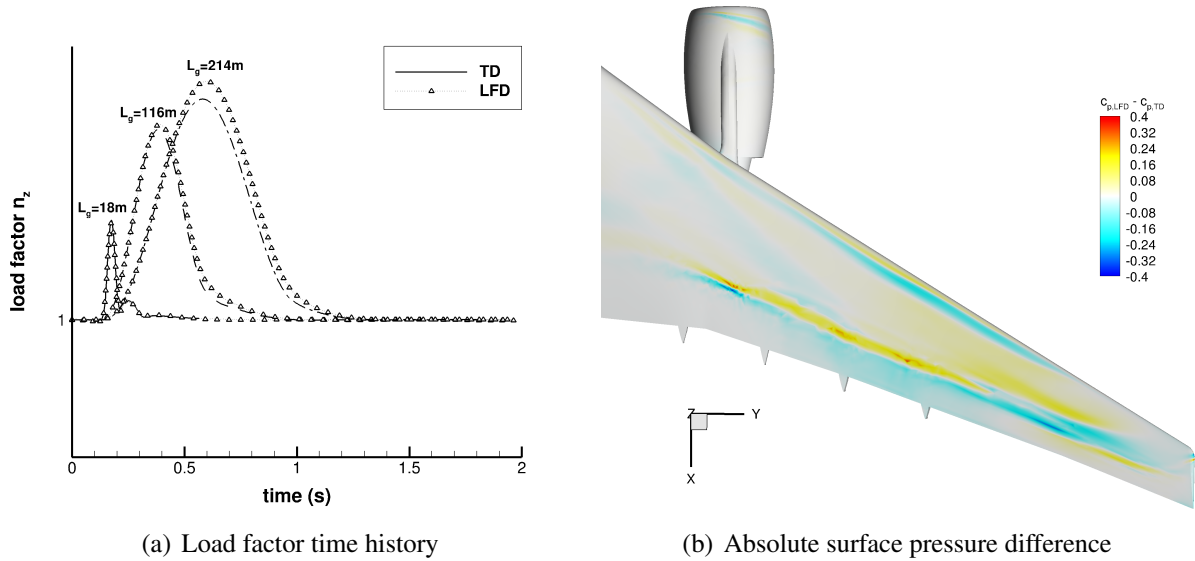


Figure 7: Time responses to several 1-cos gusts and absolute pressure differences for $L_g = 116$ m

In terms of computational cost, obtaining a single frequency domain response is about two orders of magnitude faster than the corresponding time domain solution. However, the memory required to solve the linear system increases compared to a time-marching approach. While an unsteady RANS simulation needs to be performed for each set of parameters separately, complex-valued frequency domain results can be used in a weighted incomplete inverse Fourier transform to reconstruct time responses of integrated values as well as the whole flowfield in a rapid manner. For gust excitation it is advisable to precompute around 15 discrete frequencies to investigate an arbitrary time domain signal e.g. 1-cos gusts. The resulting computational cost is still one order of magnitude below a single unsteady investigation while offering results for all dynamic gust responses at the defined flight condition.

3.2 Application According to Certification Requirements

After the investigation of numerical accuracy and computational efficiency presented above, the frequency domain gust approach is used to predict dynamic responses to 1-cos gusts in an efficient way. The linear system is solved at 15 reduced frequencies between 0 and 0.6. Responses to 1-cos gusts are obtained by applying a complex-valued weighting function as discussed in Sec. 2. The chosen gust lengths are $L_g = 18$ m, 116 m and 214 m with amplitudes as defined by the European Aviation Safety Agency in CS 25.341 [24]. Load factors are reconstructed and visualised in Fig. 7(a) for all three gust lengths. For the shortest gust length of $L_g = 18$ m excellent agreement between both methods is observed. With increasing gust length also the gust amplitude is growing, causing dynamically nonlinear responses near the maximum load factor. Since the frequency domain approach assumes a dynamically linear response, reconstructed load factors are slightly overpredicted for gust lengths of $L_g = 116$ m and 214 m. The absolute surface pressure difference for $L_g = 116$ m at maximum load factor is displayed in Fig. 7(b). The highest error occurs around the shock foot since nonlinear shock motion and a nonlinear amplitude decrease arises during the time-marching simulation. Minor differences around the leading edge at the stagnation line are also caused from the same amplitude mechanism.

4 CONCLUSIONS

This paper outlines a method for efficiently computing the aerodynamic response to gust encounter for industry-relevant test cases. The Reynolds-averaged Navier-Stokes equations are linearised to obtain responses to sinusoidal gust excitation, a method previously presented for aerofoils. Arbitrary time domain signals such as 1-cos gusts can be simulated using a complex-valued weighting in combination with superposition of responses at discrete frequencies. Computational cost is reduced by more than two orders of magnitude compared to equivalent unsteady nonlinear time-marching simulations.

The method is applied to a large civil aircraft including flow through engines, elevator and fin at transonic cruise conditions. The steady-state 1g flight shape is generated through an iterative elastic trimming procedure. Responses at various frequencies are compared to a pulse excitation, validating the method at all frequencies of industrial interest. Complex surface pressure distributions are discussed with good agreement on the wing and tail globally as well as in specific wing and elevator sections. Finally, characteristic 1-cos gusts are reconstructed and results are matched to time-marching simulations. Although results are produced for a very complex geometry including pylon and nacelles, an excellent agreement between the time and frequency domain methods is obtained. This includes the global lift coefficient as well as surface pressure distributions, thus demonstrating the maturity of the method.

Work to extend the method to generate a reduced-order model for the three-dimensional test case is currently in progress. Also, it is desirable to incorporate nonlinear aerodynamic effects to increase the accuracy of predicted loads further at transonic conditions. In addition, introducing structural and rigid-body motions in the response simulation is desirable to account for elastic surface deformation and changes in the flight path during the aircraft gust interaction.

ACKNOWLEDGEMENTS

The research leading to these results was co-funded by Innovate UK, the UK's innovation agency, as part of the Enhanced Fidelity Transonic Wing project.

REFERENCES

- [1] Albano, E. and Rodden, W. P., "A doublet lattice method for calculating lift distribution on oscillating surfaces in subsonic flow," *AIAA Journal*, Vol. 2, No. 7, 1969, pp. 279–285.
- [2] Reimer, L., Ritter, M., Heinrich, R., and Krüger, W., "CFD-based Gust Load Analysis for a Free-flying Flexible Passenger Aircraft in Comparison to a DLM-based Approach," *22nd AIAA Computational Fluid Dynamics Conference*, 2015, AIAA 2015-2455.
- [3] Thormann, R., Nitzsche, J., and Widhalm, M., "Time-linearized Simulation of Unsteady Transonic Flows with Shock-Induced Separation," *European Congress on Computational Methods in Applied Sciences and Engineering*, 2012, ECCOMAS 2012.
- [4] Bekemeyer, P. and Timme, S., "Reduced Order Gust Response Simulation using Computational Fluid Dynamics," *57th AIAA/ASCE/AHS/ASC Structures, Structural Dynamics, and Materials Conference*, 2016, AIAA 2016-1485.
- [5] Whitehead, D. S. and Grant, J. R., "Force and Moment Coefficients of High Deflection Cascades," *2nd International Symposium on Aeroelasticity in Turbomachinery*, 1981.

- [6] Verdon, J. M. and Caspar, J. R., “Development of a Linear Unsteady Aerodynamic Analysis for Finite-Deflection Subsonic Cascades,” *AIAA Journal*, Vol. 20, No. 9, 1982, pp. 1259–1267.
- [7] Verdon, J. M. and Caspar, J. R., “A Linearized Unsteady Aerodynamics Analysis for Transonic Cascades,” *Journal of Fluid Mechanics*, Vol. 149, 1984, pp. 403–429.
- [8] Hall, K. C. and Clark, W. S., “Linearized Euler Predictions of Unsteady Aerodynamic Loads in Cascades,” *AIAA Journal*, Vol. 31, No. 3, 1993, pp. 540–550.
- [9] Hall, K. C., Clark, W. S., and Lorence, C. B., “A Linearized Euler Analysis of Unsteady Transonic Flows in Turbomachinery,” *Journal of Turbomachinery*, Vol. 116, No. 3, 1994, pp. 477–488.
- [10] Mortchéléwicz, G. D., “Application des Équations d’Euler Linéarisées à la Prévision du Flottement,” *85th Meeting of the AGARD Structures and Materials Panel*, 1997, AGARD Report 822: Numerical Unsteady Aerodynamic and Aeroelastic Simulation.
- [11] Widhalm, M., Dwight, R. P., Thormann, R., and Hübner, A. R., “Efficient Computation of Dynamic Stability Data with a Linearized Frequency Domain Solver,” *5th European Conference on Computational Fluid Dynamics*, 2010, ECCOMAS CFD 2010.
- [12] Weishäupl, C. and Laschka, B., “Small Disturbance Euler Simulations for Delta Wing Unsteady Flows due to Harmonic Oscillations,” *Journal of Aircraft*, Vol. 41, No. 4, 2004, pp. 782–789.
- [13] Clark, W. S. and Hall, K. C., “A Time-Linearized Analysis of Stall Flutter,” *Journal of Turbomachinery*, Vol. 122, No. 3, 2000, pp. 467–476.
- [14] Pechloff, A. and Laschka, B., “Small Disturbance Navier-Stokes Computations for Low-Aspect-Ratio Wing Pitching Oscillations,” *Journal of Aircraft*, Vol. 47, No. 3, 2010, pp. 737–753.
- [15] Thormann, R. and Widhalm, M., “Linear-Frequency-Domain Predictions of Dynamic-Response Data for Viscous Transonic Flows,” *AIAA Journal*, Vol. 51, No. 11, 2013, pp. 2540–2557.
- [16] Thormann, R. and Widhalm, M., “Forced Motion Simulation using a Linear Frequency Domain Solver for a Generic Transport Aircraft,” *International Forum on Aeroelasticity and Structural Dynamics (IFASD)*, 2013, IFASD 2013-17A.
- [17] Parameswaran, V. and Baeder, J. D., “Indicial aerodynamics in compressible flow-direct computational fluid dynamic calculations,” *Journal of Aircraft*, Vol. 34, No. 1, 1997, pp. 131–133.
- [18] Schwamborn, D., Gerhold, T., and Heinrich, R., “The DLR TAU-Code: Recent Applications in Research and Industry,” *European Conference on Computational Fluid Dynamics*, 2006, ECCOMAS CFD 2006.
- [19] Spalart, P. R. and Allmaras, S. R., “A One-Equation Turbulence Model for Aerodynamic Flows,” *Recherche Aérospatiale*, Vol. 1, 1994, pp. 5–21.

- [20] Jameson, A., Schmidt, W., and Turkel, E., “Numerical Solutions of the Euler Equations by Finite Volume Methods Using Runge-Kutta Time-Stepping Schemes,” *AIAA Journal*, 1981, pp. 1981–1259.
- [21] Dwight, R., “An Implicit LU-SGS Scheme for Finite-Volume Discretizations of the Navier-Stokes Equations on Hybrid Grids,” *DLR-FB-2005-05*, 2006.
- [22] Xu, S., Timme, S., and Badcock, K. J., “Krylov Subspace Recycling for Linearised Aerodynamics Analysis using DLR-TAU,” *International Forum on Aeroelasticity and Structural Dynamics (IFASD)*, 2015, IFASD-2015-186.
- [23] Saad, Y., *Iterative Methods for Sparse Linear Systems*, Society for Industrial and Applied Mathematics, Philadelphia, PA, 2nd ed., 2003.
- [24] European Aviation Safety Agency, “Certification Specifications for Large Aeroplanes (CS-25),” 2015.